



Line graph theory reveals hidden spin frustration and bond frustration in molecular crystals with strong isotropy

Journal:	<i>Journal of Materials Chemistry C</i>
Manuscript ID	TC-REV-10-2021-005161.R1
Article Type:	Review Article
Date Submitted by the Author:	07-Dec-2021
Complete List of Authors:	Suizu, Rie; Nagoya University, Department of Chemistry Awaga, Kunio; Nagoya Univ.,

ARTICLE

Line graph theory reveals hidden spin frustration and bond frustration in molecular crystals with strong isotropy

Received 00th January 20xx,
Accepted 00th January 20xx

DOI: 10.1039/x0xx00000x

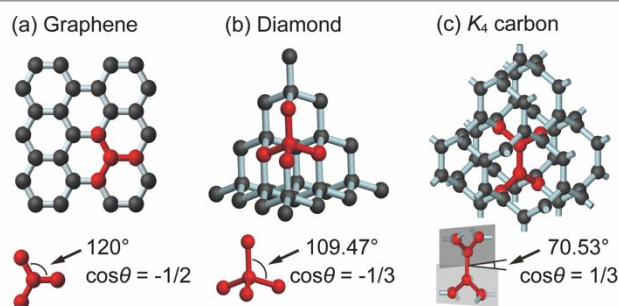
Rie Suizu^{a,b} and Kunio Awaga^a

Graph theory has demonstrated that only three lattices, namely, honeycomb, K_4 , and diamond lattices, possess a strong isotropic property. It is also recognized that their line graphs correspond to kagome, hyper-kagome, and pyrochlore lattices, respectively, which are well known as spin frustration lattices. This relation suggests that the materials with the strong isotropic lattices possess “hidden” frustration. In this review article, after introducing the strong isotropy and the line graph transformation, we describe the spin frustration and formation of the spin liquid state in a honeycomb MOF, $\text{Cu}_3(\text{HHTP})$, and in a molecule-based K_4 , (-)-NDI- Δ . We also report the unusual phase transitions in a molecule-based diamond, bpBDTDA, which are considered to result from bond frustration: specific periodical lattice distortions in the strong isotropic lattices are forbidden, in such a way that long-range antiferromagnetic orderings are forbidden in the spin frustration lattices.

1. Introduction

Strong isotropy

Carbon allotropes, such as graphite, diamond, and nanocarbons—*e.g.*, C_{60} and nanotubes—are well known to exhibit excellent electronic and mechanical properties. Recently, K_4 carbon was proposed as a new carbon allotrope based on graph theory,^{1–3} although it has not been synthesized yet. The crystal structures of graphene, diamond and K_4 carbon are shown in Scheme 1. The structure of graphene—namely, a honeycomb lattice—belongs to the hexagonal space group $P6/mmm$ with a characteristic angle of $\vartheta = 120^\circ$ ($\cos \vartheta = -1/2$). The diamond lattice belongs to the cubic space group $Fd\bar{3}m$ and the buckling six-membered rings are interconnected. All the vertices are at the centre of the tetrahedron formed by the four neighbouring atoms with an angle of $\vartheta = 109.47^\circ$ ($\cos \vartheta = -1/3$). The K_4 lattice is a chiral structure, belonging to the cubic space group $I4_132$. This lattice consists of interconnected ten-membered rings with a huge cavity. Each lattice point exists at the centre of a triangle formed by the three neighbouring atoms. The neighbouring triangles, which share one bond, are twisted with a dihedral angle $\vartheta = 70.53^\circ$ ($\cos \vartheta = 1/3$). It is notable that the band structures of the three allotropes are unique and attractive; those of graphene, K_4 carbon, and diamond are theoretically demonstrated to possess Dirac cones, triplet Dirac cones, and Dirac nodal lines, respectively.^{4–6}



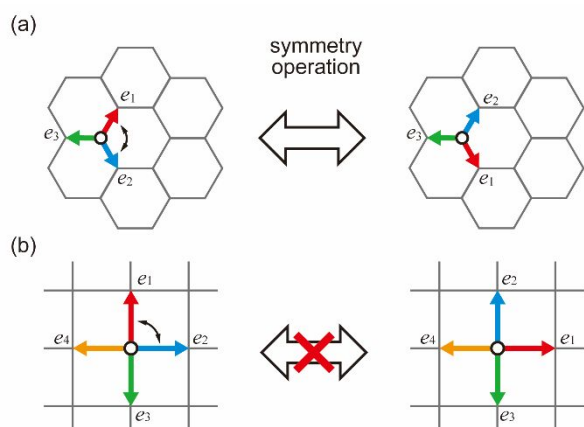
Scheme 1 Crystal structures of graphene (a), diamond (b), and K_4 carbon (c).

It is mathematically proved that only honeycomb, diamond and K_4 lattices possess a special symmetry called “strong isotropy”.^{1–3} As shown in Scheme 2(a), the honeycomb lattice consists of three bonds (red, blue and green) that are oriented in different directions. Any bond swapping, *e.g.*, between red and blue, can be explained by a symmetry operation. This is the strong isotropy that preserves the crystal net after any permutation of edges with a common vertex. In contrast, the square lattice does not exhibit this property, as shown in Scheme 2(b). It is said that crystallographic symmetry is determined only by atomic positions, but the strong isotropy is governed by both atomic and bond positions. The honeycomb, diamond and K_4 lattices are characterized by the specific angles: $\cos \vartheta = -1/2$, $-1/3$, and $+1/3$, respectively. The inclusion of the numbers 2 and 3 in these expressions is due to these being 2D and 3D lattices with very high isotropy. Since $\cos \vartheta$ for the diamond and K_4 lattices are $-1/3$ and $+1/3$, respectively, they are called “mathematical twins”. Although the visibility of the K_4 lattice is

^a Department of Chemistry & Integrated Research Consortium on Chemical Sciences (IRCCS), Nagoya University, Furo-cho, Chikusa-ku, Nagoya 464-8602, Japan.

^b Japan Science and Technology Agency (JST), PRESTO, 4-1-8 Honcho, Kawaguchi, Saitama, 332-0012, Japan

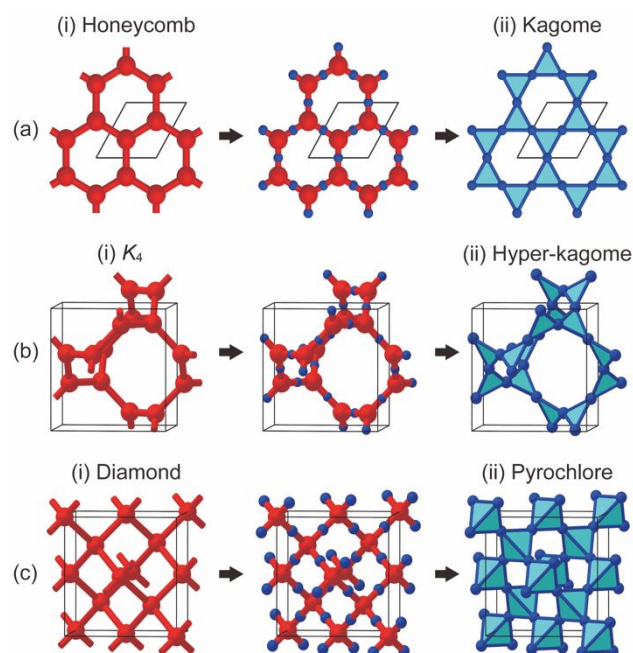
much less than that of the diamond lattice, the K_4 lattice is a universal material structure which appears in various scales.⁴



Scheme 2 Comparison between the honeycomb lattice (a) and square lattice (b). In the former, bond swapping between the blue and red edges can be expressed by the symmetry operation, but in the latter, this is not the case.

Line graph

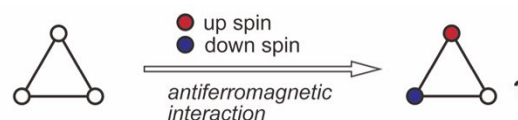
Next, we will discuss the line graphs of the strongly isotropic lattices. The first column in Scheme 3 shows honeycomb, K_4 and diamond lattices. In the second column, a small blue atom is added on each bond. By drawing bonds between the blue atoms, the original three lattices are transformed into the kagome, hyper-kagome and pyrochlore lattices, respectively, as shown in the third column in Scheme 3. It is notable that these three lattices are well recognized as spin frustration lattices.



Scheme 3 Line graphs of the strong isotropic lattices, honeycomb, K_4 and diamond. Panels (a), (b) and (c) show their transformations toward the spin frustration lattices, kagome, hyper-kagome and pyrochlore, respectively.

2. Spin frustration in molecular honeycomb and K_4 lattices

Geometrical frustration has been recognised as the result of an intrinsic incompatibility between certain fundamental interactions and the underlying lattice geometry. The spin frustration is the best-known example. A simple example of spin frustration is an antiferromagnetically coupled three-spin system on a triangle (Scheme 4). In this section, we will introduce our recent researches on spin frustration, which can be well understood by the line graph theory for the strongly isotropic lattices.



Scheme 4 Spin frustration in a triangle.

Honeycomb MOF

Figure 1(a) shows the crystal structure of a semiconductive 2D MOF, $\text{Cu}_3(\text{HHTP})_2$ (HHTP = hexahydroxytriphenylene),⁷ where the inset shows the molecular structure of HHTP. The structure consists of a honeycomb lattice formed by the coordination bonds between the triangular HHTP ligands and the Cu(II) ions with $S = 1/2$. Since the Cu(II) ion exists at the midpoint on each bond of the honeycomb MOF network, the Cu(II) ions form a 2D kagome lattice (Fig. 1(b)) with a Cu(II)-Cu(II) distance of ~ 11 Å.

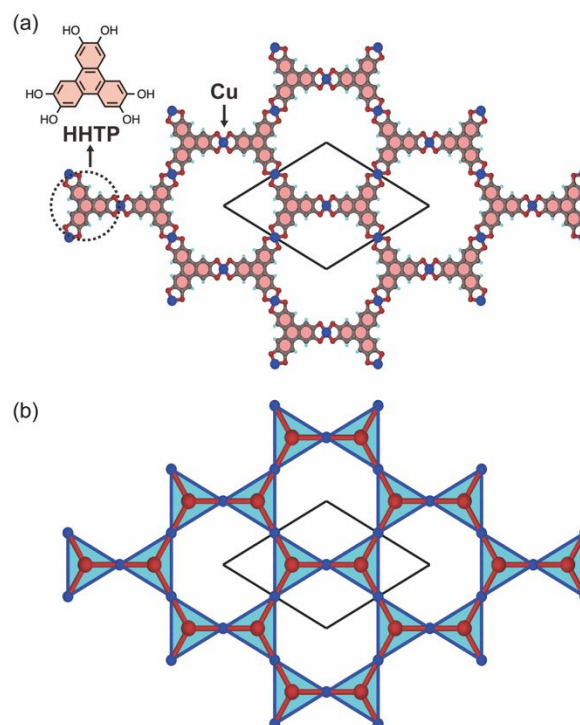


Figure 1. Crystal structure of a 2D MOF, $\text{Cu}_3(\text{HHTP})_2$ (a), in which the red spheres (HHTP ligand) form a honeycomb lattice, and the blue spheres ($S = 1/2$ Cu(II)) form a kagome lattice (b).

Figure 2(a) shows the temperature dependence of the paramagnetic susceptibility of $\text{Cu}_3(\text{HHTP})_2$ down to 38 mK.⁸ Above 2 K, the temperature dependence follows the Curie-Weiss law with a negative Weiss constant of $\vartheta = -3.4$ K, indicating a dominant antiferromagnetic interaction between the Cu(II) ions. This interaction should bring about spin frustration on the Cu(II) kagome lattice. In fact, in spite of this interaction, the magnetic susceptibility shows a gradual increase down to 38 mK, without indicating any long-range magnetic ordering.

Figure 2(b) shows the temperature dependence of the specific heat capacity of $\text{Cu}_3(\text{HHTP})_2$, namely, c_p/T vs. T^2 plots in the temperature range between 65 mK and 20 K. Below 7 K, the values of c_p/T show an abrupt increase, which is attributable to a high-temperature-side tail of a Schottky anomaly induced by paramagnetic lattice defects and/or nuclear spins. Above 7 K, the temperature dependence can be fit to the equation, $c_p = \gamma T + \beta T^3$. The values of γ and β are shown in Fig. 2(b). The non-zero γ value, namely, the presence of a large heat capacity at low temperatures, indicates the formation of a spin liquid state, induced by the spin frustration in this MOF.

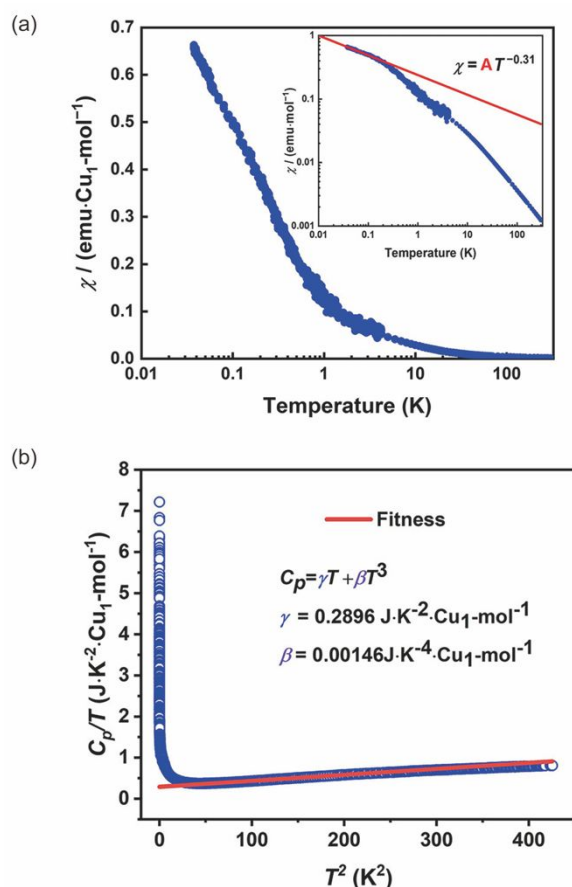


Figure 2 (a) Temperature dependence of the magnetic susceptibility of $\text{Cu}_3(\text{HHTP})_2$ down to 38 mK. (b) C_p/T - T^2 plot for $\text{Cu}_3(\text{HHTP})_2$ in the temperature range of 0.065–20 K. Adapted with permission from ref. 8. Copyright 2020 American Chemical Society.

Molecular K_4 lattice

The naphthalene diimide trimer, NDI- Δ (Fig. 3(a)), is a chiral molecule, and consists of three π -conjugated planes whose

normal vectors (red arrows) intersect each other at 120° .^{9–19} This molecule exhibits reversible six-step reductions on the CV curves due to the strong acceptor ability of the NDI moiety.⁹ Although there was no specific intermolecular interaction in the crystal structure of the neutral species of NDI- Δ , we attempted to form a supramolecular K_4 lattice through the formation of π - π pancake overlap due to an exchange interaction between the anion radical species of NDI- Δ .

Figure 3(c-i) shows the molecule-based K_4 lattice found in the crystal structures of $[\text{Cat}]_3[(-)\text{NDI-}\Delta]_2$ with Cat = alkali metal ions, ammonium cations, phosphonium cations ..., which were prepared by galvanostatic reduction.^{4,20–22} All the crystals are formed by a π - π pancake overlap shown in Fig. 3(b), and belong to cubic system with nearly the same lattice parameter ($a = 20.9$ – 30.9 Å). This composition ratio means that $(-)\text{NDI-}\Delta$ has a charge of -1.5 per molecule, and each NDI π -plane has a charge of -0.5 . The calculated values of the intra- and intermolecular transfer integrals are $t_1 = -0.029$ eV and $t_2 = -0.258$ eV, respectively.²⁰

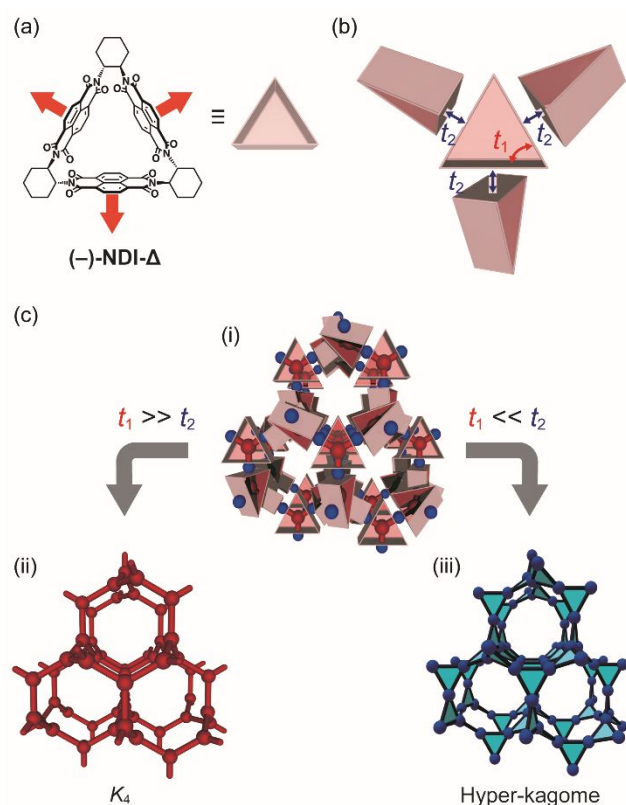


Figure 3 (a) Molecular structure of $(-)\text{NDI-}\Delta$, (b) nearest-neighbour intermolecular arrangement, and (c) a schematic view of the crystal structure of $[\text{Cat}]_3[(-)\text{NDI-}\Delta]_2$ (i), the K_4 structure, formed by the centroids of $(-)\text{NDI-}\Delta$ molecules (ii) and the hyper-kagome lattice, which in turn is formed by the unpaired electrons (iii).

The intermolecular interaction in $[\text{Cat}]_3[(-)\text{NDI-}\Delta]_2$ t_2 is about one order of magnitude stronger than the intramolecular interaction t_1 . In addition, one NDI plane has a negative charge of -0.5 . Therefore, it is reasonable to conclude that an unpaired electron exists at the midpoint of the intermolecular π -dimer (blue circle in Fig. 3(c-i)). This feature is similar to the Mott dimer system in the BEDT-TTF salts.²³ As is discussed in Scheme

3(b), the (–)-NDI- Δ molecule forms a K_4 lattice (Fig. 3(c-ii)), and the unpaired electrons form the line graph of this lattice, namely, a hyper-kagome lattice that is expected to exhibit spin frustration (Fig. 3(c-iii)). To our knowledge, this system is the first hyper-kagome lattice formed by organic Heisenberg spins. Figure 4(a) shows the temperature dependence of the paramagnetic susceptibility χ_p in the temperature range 0.07–300 K for $[\text{N}(\text{C}_4\text{H}_9)_4]_{1.5}[(\text{–})\text{-NDI-}\Delta]$.²¹ χ_p increases with decreasing temperature and exhibits a small anomaly around 20 K, which is probably caused by the interdimer interaction. The data indicate no long-range magnetic ordering despite the 3D antiferromagnetic interactions. Below 0.2 K, the magnetic behaviour can be explained by $\chi_p = \chi_0 + \chi_{\text{def}}$ with $\chi_{\text{def}} = C_{\text{def}}/(T - \theta_{\text{def}})$, where χ_0 , χ_{def} , C_{def} and θ_{def} are the constant paramagnetic susceptibility, the paramagnetic susceptibility caused by the lattice defects, the Curie constant and the Weiss temperature for the lattice defects, respectively. The contribution from defect spins can be estimated at 9.6% from fitting parameters. The red curve in Figure 4(a) is the intrinsic paramagnetic susceptibility χ_{int} , which is calculated by $\chi_{\text{int}} = \chi_p - \chi_{\text{def}}$. The results of this analysis clearly suggest the presence of χ_{int} even at 0.5K, despite the 3D magnetic interactions.

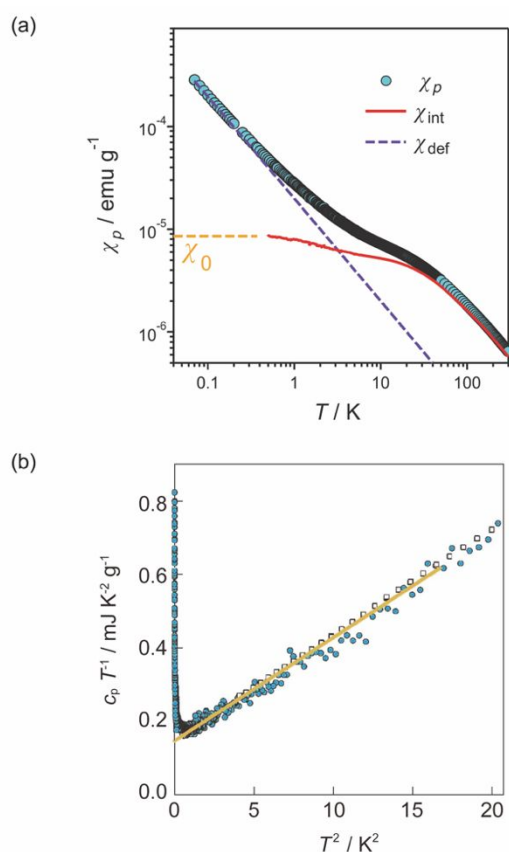
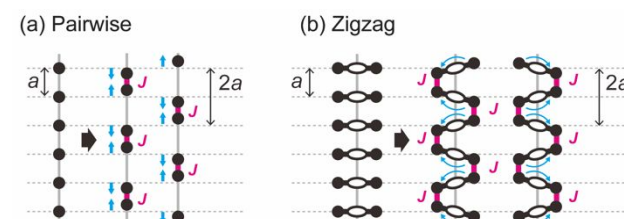


Figure 4 (a) Temperature dependence of the paramagnetic susceptibility χ_p in the temperature range 0.07–300 K for $[\text{N}(\text{C}_4\text{H}_9)_4]_{1.5}[(\text{–})\text{-NDI-}\Delta]$. The purple broken line and the red curve indicate the temperature dependences of χ_{def} and χ_{int} , respectively. See the text. (b) Temperature dependence of the heat capacity for $[\text{N}(\text{C}_4\text{H}_9)_4]_{1.5}[(\text{–})\text{-NDI-}\Delta]$ in the plots of c_p/T vs. T^2 . Adapted with permission from ref. 21. Copyright 2017 American Physical Society.

Figure 4(b) shows the temperature dependence of heat capacity. The increase below ca. 0.1 K is an extrinsic Schottky anomaly. The large extrapolation value from the high temperature side at absolute zero suggests that a large degree of freedom remains at the extremely low temperature. Based on this feature, we concluded the formation of the spin liquid ground state.

3. Bond frustration

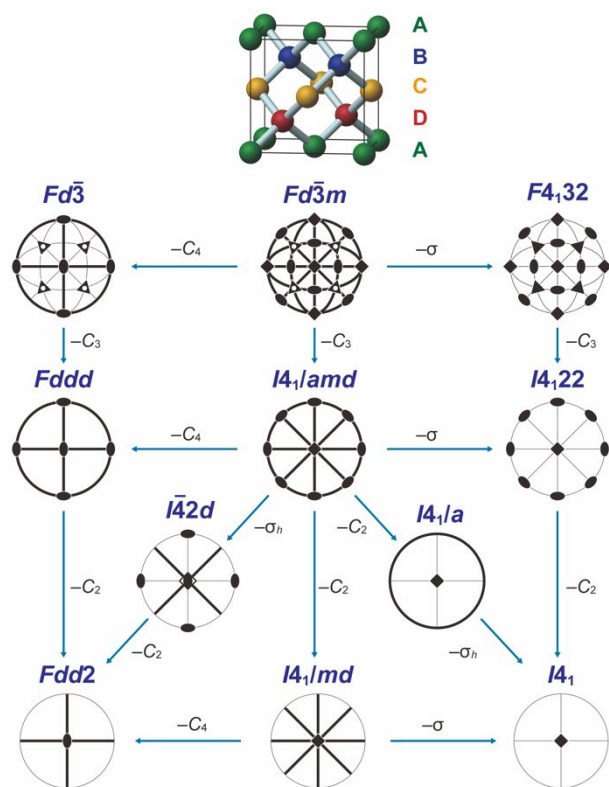
In this section, we describe a hidden “bond frustration” in the crystals of an organic biradical bpBDTDA (inset of Figure 5), which include a molecule-based diamond structure.²⁴ Organic radicals often exhibit the phase transitions accompanied with the lattice modulation, such as the dimerization, reflecting their strong electron/spin-lattice interactions. Scheme 5(a) illustrates the pairwise dimerization accompanied with the movement of the molecular centroids. However, bpBDTDA having a bulky moiety exhibits a zigzag dimerization without a centroid shift, as shown in Scheme 5(b). We describe the stepwise, spatially-inhomogeneous phase transitions toward zigzag dimerization in bpBDTDA in terms of bond frustration, which is predicted by the line graph of diamond lattice.



Scheme 5 Dimerization patterns in organic radicals: (a) pairwise, (b) zigzag.

Molecular diamond: Crystal structure of bpBDTDA at 400 K

The crystal structure of bpBDTDA at 400 K belongs to the orthorhombic space group $Fdd2$. Before discussing the crystal structure of bpBDTDA, we will explain the relation between this lattice and diamond lattice. In general, the crystal structure is determined by the lattice and its basis. The diamond structure (inset of Scheme 6) consists of four layers of basis, **A–D**, whose heights are shifted by 1/4 of the lattice length. It is noted that the basis in layer **A** is bonded to two bases in each of layers **D** and **B**, the basis in layer **B** to two bases in each of **A** and **C**, the basis in layer **C** to two bases in each of **B** and **D**, and the basis in layer **D** to two bases in each of **C** and **A**. Scheme 6 shows the space groups of the lattices, which are relevant to the space group of diamond, $Fd-3m$. By reducing symmetry stepwisely, the other ten space groups are obtained, among which the space group $Fdd2$ for bpBDTDA is the least symmetric.



Scheme 6 Correlation between the symmetry of basis and space groups in the diamond lattice.

Figure 5 shows the crystal structure of bpBDTDA at 400 K, in which the crystallographically-independent unit is a half of the bpBDTDA molecule (Figure 5(a)). The molecular structure is axially chiral due to the steric hindrance in the biphenylene rings (Figure 5(b)). As shown in the *c*-axis projection (Figure 5(c)), the unit cell contains four molecules, **A–D**. The fractional coordinates of these **A–D** molecules in the *c* axis are shifted by 1/4. The two light blue dashed lines at the ends of the molecules indicate the intermolecular short S...N or S...S contacts. These intermolecular short contacts along the four directions are crystallographically equivalent, and form the diamond network. This means that **A** or **C** forms the short contacts with **B** and **D**, but there is a steric repulsion between the biphenylene rings of **A** and **C**, despite the fact that **A** and **C** neighbour each other along the *a* axis. This feature is the same for **B** or **D** with respect to **A** and **C**. Due to steric effects between the biphenylene rings, the molecular centroids of **A** and **C** are shifted by 1/2 along the *c* axis. To make side-by-side short contacts between the radical moieties, the molecular centroids of **B** and **D** are located at the midpoint between **A** and **C**, namely at 1/4 and 3/4. This intermolecular contact is defined as a "diamond bond". Figure 6(a) show the stacking modes in the four columns, **A**, **B**, **C** and **D**. The crucial difference between diamond and this molecular crystal is that each of the four bpBDTDA molecules (**A–D**) forms a one-dimensional π -stacked column along the *c* axis, which is formed by a π - π face-to-face overlap between the dithiadiazolyl rings with a constant interplanar distance of 3.6419(8) Å (Figure 6(a)).

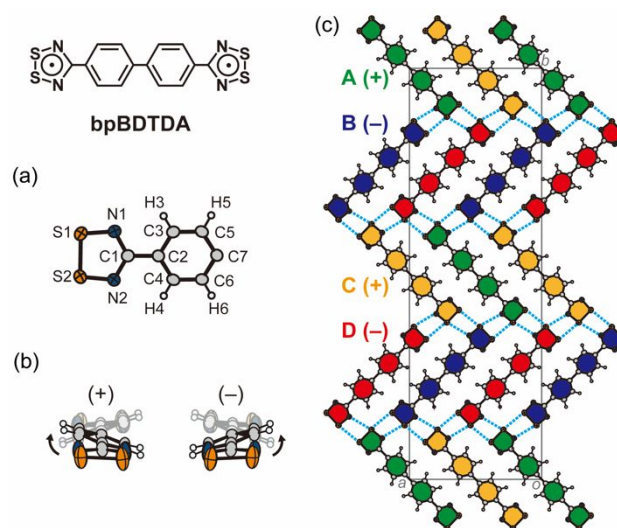


Figure 5 Crystal structures of bpBDTDA at 400 K in the HT phase. (a) An asymmetry unit, (b) (+) and (-) enantiomers, (c) *c* axis projection of the unit cell.

Stepwise and spatially inhomogeneous phase transitions: Crystal structures in the IT and LT phases

Figure 6(b) shows the results of differential scanning calorimetry (DSC), which clearly indicated the presence of two successive phase transitions with latent heat changes at 359 K and 306 K without hysteresis. The enthalpy changes at the two temperatures are $\Delta H = 179$ and 52.3 J mol^{-1} , respectively, with a ratio of about 3:1. It is concluded that bpBDTDA exhibits three phases: a high temperature (HT) phase above 359 K, a low temperature (LT) phase below 306 K, and an intermediate temperature (IT) phase between these temperatures. Upon cooling, a two-step first-order phase transition was observed with lattice dimerization. In the IT and LT phases, the crystal structures belong to the same monoclinic space group $P2_1$. The unit cell consists of four crystallographically independent molecules **A–D**, which can be corresponded to those in the HT phase. In the IT phase, strangely enough, three columns **A–C** undergo alternating dimerization to form zigzag π stackings along the monoclinic *b* axis, while column **D** keeps uniform stacking (Figure 6(a)). After further cooling to the LT phase, there is no change in the zigzag dimerization pattern of columns **A–C**, but the last remaining column **D** undergoes zigzag dimerization. This heterogeneous zigzag dimerization with a 3:1 ratio is consistent with the enthalpy change.

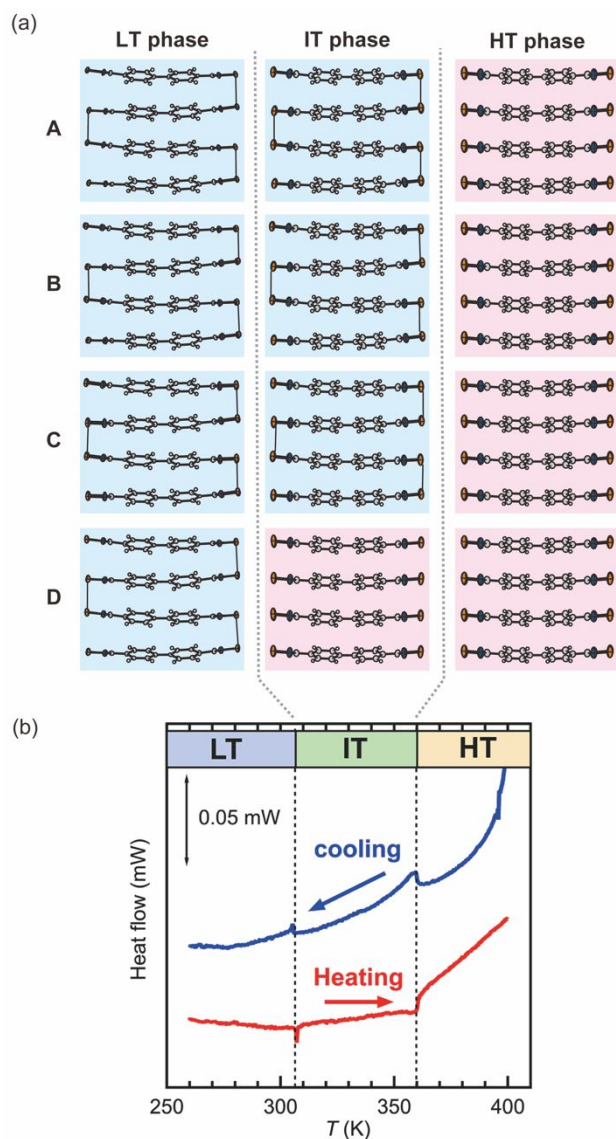


Figure 6 (a) The stacking modes in the four columns, **A**, **B**, **C** and **D**, in the three phases; a pink background indicates uniform stacking, while a blue one indicates zigzag dimerization. (b) DSC curves upon heating (red curve) and cooling (blue curve) in the temperature range between 260 and 400 K.

Figure 7(a) shows the temperature dependence of the intracolumnar, intermolecular S...S distances of the four stacking columns, **A–D**. These distances are defined in the inset of this figure. In the HT phase above 359 K, there is only one S...S distance, which indicates that columns **A–D** are crystallographically identical and uniformly stacked. In the IT phase between 306 and 359 K, the S...S distances of columns **A–C** can be clearly classified into two groups, the shorter ones (*ca.* 3.2 Å) and the longer ones (*ca.* 3.9 Å). In the LT below 306 K, the remaining column **D** also undergoes the zigzag dimerization. The ratio of the uniform stacking column to the zigzag dimerization column changes in a spatially inhomogeneous and stepwise manner as the temperature decreases. In addition, Figure 7(b) shows the temperature dependence of coordinate shift Δx of the molecular centroid along the π -stacking direction. It is noted that the zigzag dimerization can occur without the

centroid shift, as shown in Scheme 5(b). In the HT phase, molecules **A–D** are located at $x = 0.00, 0.25, 0.50,$ and 0.75 in the diamond lattice, respectively. In the IT phase, where zigzag dimerization occurs in columns **A–C**, there is no significant change in the molecular centroids. However, in the LT phase the centroids of all molecules change remarkably. It is very strange that this ratio in the IT phase is 3:1 instead of 1:1 and that the zigzag dimerization, which does not require any change in the molecular centroids, results in a large centroid shift in the LT phase.

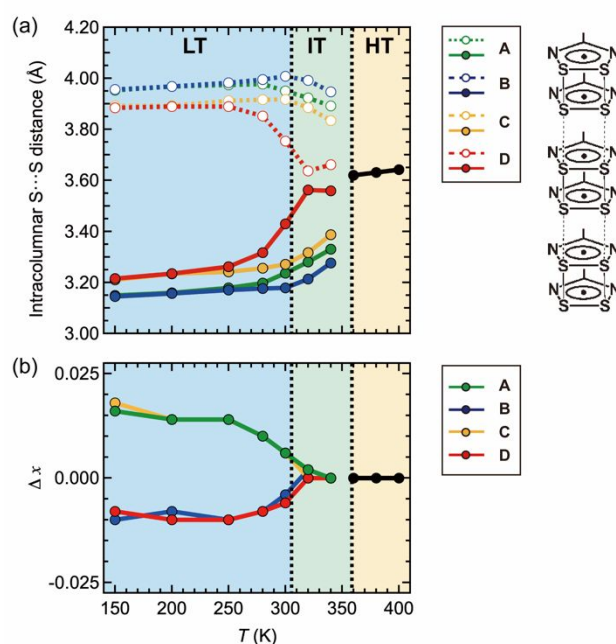


Figure 7 Temperature dependence of the intracolumnar and intermolecular S...S distances in the four stacking columns (a) and the displacements of the centroid positions Δx for molecules **A**, **B**, **C**, and **D** from $x=0, 0.25, 0.5,$ and 0.75 , respectively, with respect to the c axis in the HT phase and the b axis in the IT and LT phases.

Hidden bond frustration in diamond lattice

In this section, we discuss the zigzag dimerization in the diamond network of bpBDTDA. Figure 8(a) shows the structural displacement of molecule **A** and its correlation to molecules **B** and **D** in the zigzag dimerization. Molecule **A** is connected to two molecules **B**, which are shifted by $+1/4$ along the c axis, and is also connected to two molecules **D**, which are shifted by $-1/4$ along the c axis, in the direction perpendicular to the **B–A–B** direction. For clarity, the diagram is divided into an upper and lower panel. The four diamond bonds in the HT phase (namely, before dimerization, Figure 8(a-i)) are coloured white to show that they are equivalent. Note that, as described in Scheme 3, the line graph of the diamond lattice is a pyrochlore lattice. Therefore, the lattice points of the pyrochlore lattice exist on the bonds in the diamond lattice. After dimerization, there is a zigzag dimerization of columns **B** and **D** associated with the zigzag dimerization of column **A**. As shown in Scheme 5(b), there are two zigzag dimerization patterns, which are energetically equivalent. However, the zigzag dimerization pattern of columns **B** and **D** can be uniquely determined by the

rule that the molecules should be placed as close to each other as possible—that is, that the intermolecular interactions should be shortened. In other words, as column **A** is deformed, columns **B** and **D** are deformed so that the radical moieties are closer together. Figure 8(b) shows a schematic presentation of this structural change of one molecule: a tetrahedron model is chosen to express the molecular displacement in the phase transition, where the large grey sphere expresses a bpBDTDA molecule, forming a diamond network, and the small spheres, forming pyrochlore, express the bonds in the diamond lattice. The absence of colour on the pyrochlore lattice points means that the four intermolecular contacts are equivalent, as found in the HT phase. In the phase transition to the IT/LT phases, the midpoint of the intermolecular interaction around one molecule becomes inequivalent; two of the four move upward and the other two move downward with respect to the stacking direction. Figures 8(c) and (d) show the correlated displacement of five molecules that are connected by the intermolecular contacts, and its tetrahedron model, respectively.

Let us consider the local structural deformation, described in Figure 8, in a whole diamond/pyrochlore lattice, as shown in Figure 9. Figure 9(a) shows a diamond/pyrochlore lattice in which one **A-B-C-D-A** connection is emphasized using colour. The zigzag dimerization along the *c* axis requires an antiphase for the zigzag patterns of tetrahedra **A** at $x = 0$ and tetrahedra **A** at $x = 1$ (Figure 9(b)). If the acceptable red and blue patterns shown in Figure 8(b) are applied to the remaining **B** and **C** tetrahedra in sequence, a frustration—namely, a mismatch in the red-blue pattern—arises in **D**, as shown in Figure 9(c). In other words, the diamond structure is not consistent with the zigzag dimerization along the *c* axis. We believe that this frustration led to the spatially inhomogeneous stepwise phase transitions observed in this system, as well as to the shifting of the molecular centroids in order to achieve the zigzag dimerization observed in the LT phase.

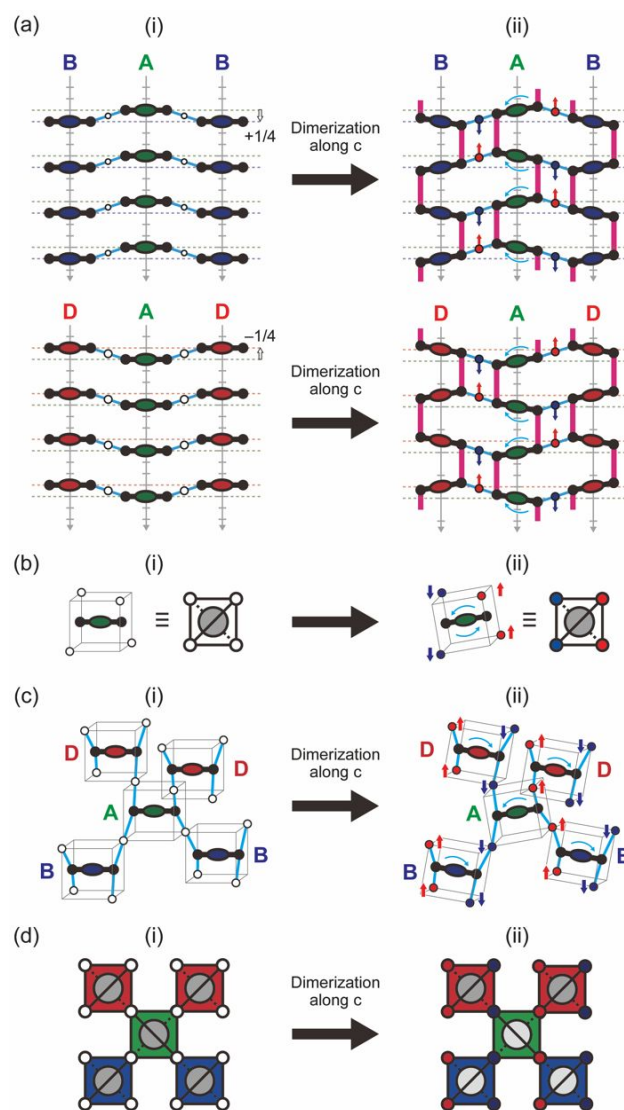


Figure 8 Schematic illustrations of the structural transition from the regular stacking in the HT phase (i) to the zigzag stacking in the IT/LT phases (ii); (a) Side views for the structural relations between the stackings, **A** and **B**, and between **A** and **D**. (b) Displacement of one molecule. This panel also shows the tetrahedron model to express the displacement of one molecule. (c) Correlated displacement of five molecules, connected by the intermolecular contacts. (d) Tetrahedron model for the correlated displacement of the five molecules in panel (c).

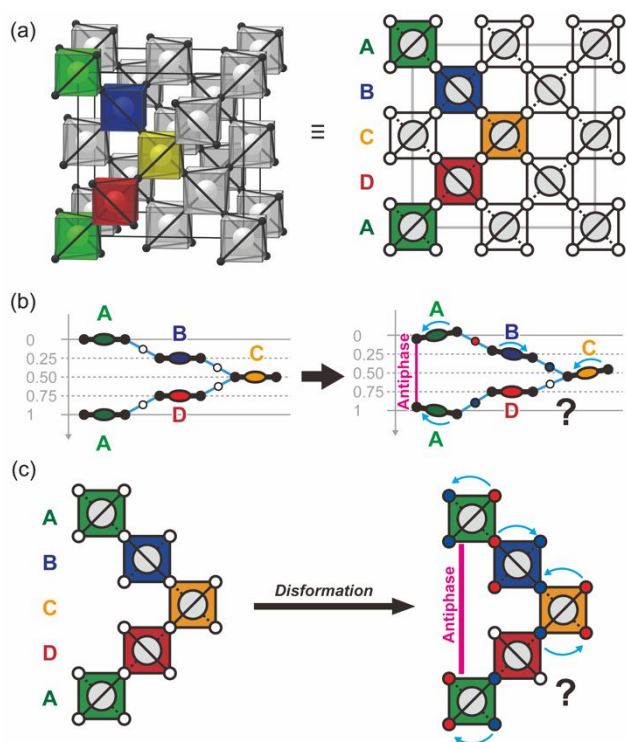


Figure 9 Bond frustration in the diamond lattice induced by the lattice modulation; (a) Schematic view and tetrahedron model of the diamond/pyrochlore lattice. In the tetrahedron model, the grey and white circles represent the positions of the molecular centroid and intermolecular interactions, respectively. The coloured tetrahedra A-B-C-D-A, connected in this order, are related by a 4-fold screw axis. (b) Side view of the molecular displacement in the zigzag dimerization along the c axis, which suggests bond frustration in the intermolecular interaction between molecules C and D. (c) Tetrahedron model of the bond frustration in panel (b).

Summary

Although there is no obvious frustration in the strongly isotropic lattices—i.e., the honeycomb, K_4 and diamond lattices—they involve hidden frustrations, which can be recognized by their line graphs in mathematical graph theory. Namely, the line graphs of the three lattices are kagome, hyper-kagome and pyrochlore lattices, respectively. The crystal structure of semiconductive 2D MOF, $\text{Cu}_3(\text{HHTP})_2$, consisted of a kagome network, formed by Cu(II) and HHTP ligands, but in this network, the magnetic Cu(II) ions formed the kagome lattice with spin frustration. In the crystal structure of $[\text{Cat}]_3[(-)\text{-NDI-}\Delta]_2$, $[(-)\text{-NDI-}\Delta]$ formed a K_4 lattice, in which the unpaired electrons formed a hyper-kagome lattice. The low-temperature physical measurements for $\text{Cu}_3(\text{HHTP})_2$ and $[(-)\text{-NDI-}\Delta]$ indicated spin-frustration, which resulted in formation of the quantum spin liquid states. An organic biradical bpBDTDA crystallized into a diamond network structure in the HT phase, and exhibited stepwise, spatially inhomogeneous zigzag-dimerization upon cooling. This unusual transition was interpreted in terms of bond frustration, which was induced by a mismatch between crystallographic diamond symmetry and structural dimerization. The line-graph discussion was found to reveal hidden spin frustration and bond frustration in the molecular crystals with strong isotropy.

Conflicts of interest

There are no conflicts to declare.

Acknowledgements

This study was supported by Japan Society for the Promotion of Science (JSPS) KAKENHI Grants (JP20H02707 and JP20H05621) and JST, PRESTO Grant Number JPMJPR21A9, Japan.

Notes and references

- 1 T. Sunada, *Not. Am. Math. Soc.*, 2008, **55**, 208–215.
- 2 M. Itoh, M. Kotani, H. Naito, T. Sunada, Y. Kawazoe and T. Adschiri, *Phys. Rev. Lett.*, 2009, **102**, 055703.
- 3 T. Sunada, *Topological Crystallography with a View Towards Discrete Geometric Analysis* (Springer, New York, 2013).
- 4 A. Mizuno, Y. Shuku and K. Awaga, *Bull. Chem. Soc. Jpn.*, 2019, **92**, 1068–1093.
- 5 M. Tsuchiizu, *Phys. Rev. B*, 2016, **94**, 195426.
- 6 Y. Shuku, A. Mizuno, R. Ushiroguchi, C. S. Hyun, Y. J. Ryu, B.-K. An, J. E. Kwon, S. Y. Park, M. Tsuchiizu and K. Awaga, *Chem. Comm.*, 2018, **54**, 3815–3818.
- 7 R. W. Day, K. Bediako, M. Razaee, L. R. Parent, G. Skorupskii, M. Q. Arguilla, C. H. Hendon, I. Stassen, N. C. Gianneschi, P. Kim and M. Dincă, *ACS Cent. Sci.*, 2019, **5**, 1959–1964.
- 8 Y. Misumi, A. Yamaguchi, Z. Zhang, T. Matsushita, N. Wada, M. Tsuchiizu and K. Awaga, *J. Am. Chem. Soc.*, 2020, **142**, 16513–16517.
- 9 S. T. Schneebeli, M. Frascioni, Z. Liu, Y. Wu, D. M. Gardner, N. L. Strutt, C. Cheng, R. Carmieli, M. R. Wasielewski, J. F. Stoddart, *Angew. Chem. Int. Ed.*, 2013, **52**, 13100–13104.
- 10 Z. Liu, G. Liu, Y. Wu, D. Cao, J. Sun, S. T. Schneebeli, M. S. Nassar, C. A. Mirkin, J. F. Stoddart, *J. Am. Chem. Soc.*, 2014, **136**, 16651–16660.
- 11 Y. Wu, S. K. M. Nalluri, R. M. Young, M. D. Krzyaniak, E. A. Margulies, J. F. Stoddart, M. R. Wasielewski, *Angew. Chem. Int. Ed.*, 2015, **54**, 11971–11977.
- 12 D. Chen, A.-J. Avestro, Z. Chen, J. Sun, S. Wang, M. Xiao, Z. Erno, M. M. Algaradah, M. S. Nassar, K. Amine, Y. Meng, J. F. Stoddart, *Adv. Mater.*, 2015, **27**, 2907–2912.
- 13 Z. Liu, J. Sun, Y. Zhou, Y. Zhang, G. Y. Wu, S. K. M. Nalluri, Y. Wang, A. Samanta, C. A. Mirkin, G. C. Schatz, J. F. Stoddart, *J. Org. Chem.*, 2016, **81**, 2581–2588.
- 14 S. K. M. Nalluri, Z. Liu, Y. Wu, K. R. Hermann, A. Samanta, D. J. Kim, M. D. Krzyaniak, M. R. Wasielewski, J. F. Stoddart, *J. Am. Chem. Soc.*, 2016, **138**, 5968–5977.
- 15 Y. Wu, M. D. Krzyaniak, J. F. Stoddart, M. R. Wasielewski, *J. Am. Chem. Soc.*, 2017, **139**, 2948–2951.
- 16 Z. Liu, S. K. M. Nalluri, J. F. Stoddart, *Chem. Soc. Rev.*, 2017, **46**, 2459–2478.
- 17 S. K. M. Nalluri, J. Zhou, T. Cheng, Z. Liu, M. T. Nguyen, T. Chen, H. A. Patel, M. D. Krzyaniak, W. A. Goddard III, M. R. Wasielewski and J. F. Stoddart, *J. Am. Chem. Soc.*, 2019, **141**, 1290–1303.
- 18 Y. Beldjoudi, A. Narayanan, I. Roy, T. J. Pearson, M. M. Cetin, M. T. Nguyen, M. D. Krzyaniak, F. M. Alsubaie, M. R. Wasielewski, S. I. Stupp and J. F. Stoddart, *J. Am. Chem. Soc.*, 2019, **141**, 17783–17795.
- 19 Y. Wang, H. Wu, P. Li, S. Chen, L. O. Jones, M. A. Mosquera, L. Zhang, K. Cai, H. Chen, X.-Y. Chen, C. L. Stern, M. R. Wasielewski, M. A. Ratner, G. C. Schatz and J. F. Stoddart, *Nat. Commun.*, 2020, **11**, 4633.
- 20 A. Mizuno, Y. Shuku, R. Suizu, M. M. Matsushita, M. Tsuchiizu, D. R. Mañeru, F. Illas, V. Robert and K. Awaga, *J. Am. Chem. Soc.*, 2015, **137**, 7612–7615.

Journal Name

ARTICLE

- 21 A. Mizuno, Y. Shuku, M. M. Matsushita, M. Tsuchiizu, Y. Hara, N. Wada, Y. Shimizu and K. Awaga, *Phys. Rev. Lett.*, 2017, **119**, 057201.
- 22 A. Mizuno, Y. Shuku, R. Suizu, M. Tsuchiizu and K. Awaga, *CrystEngComm*, 2021, **23**, 5053–5059.
- 23 Y. Shimizu, K. Miyagawa, K. Kanoda, M. Maesato, G. Saito, *Phys. Rev. Lett.*, 2003, **91**, 107001.
- 24 R. Suizu, A. Iwasaki, Y. Shuku and K. Awaga, *J. Mater. Chem. C*, 2015, **3**, 7968–7977.